2026 Nepal rock-ice avalanche, debris flow and flash flood: preliminary assessment

Ching-Ying Tsou[1] (tsou.chingying@hirosaki-u.ac.jp), Daisuke Higaki[2] (dhigakijphu@yahoo.co.jp), Naoto Koiwa[3] (koiwa@hirosaki-u.ac.jp), Hiroshi Yagi[4] (trans_himalaya@me.com), Masahiro Chigira[5] (chigira@fgi.or.jp), Mio Takahashi[6] (soumi.ho22@gmail.com), Shanmukhesh Chandra Amatya[7] (amatyasc@gmail.com), Subodh Dhakal[8] (dhakalsubodh@gmail.com)

1 Faculty of Agriculture and Life Science, Hirosaki University
2 Okuyama Boring Co., Ltd.
3 Graduate School of Sustainable Community Studies, Hirosaki University
4 Nippon Koei Co.,Ltd.
5 Fukada Geological Institute
6 Faculty of Education, Iwate University
7 Nepal Development Research Institute
8 Department of Geology, Tri-Chandra Campus, Tribhuvan University

Highlights:

- Satellite imagery enabled rapid interpretation of the 2026 Nepal disaster.
- The event involved cascading glacier–bedrock failure and a sediment-rich flood.
- Glacier retreat and fractured bedrock may have preconditioned the slope for failure.
- The disaster caused major geomorphic changes, infrastructure damage, and secondary hazards.

1. Overview

On 26 August 2026, a catastrophic rock-ice avalanche and flash flood occurred near the Nepal–China border. The disaster was initiated by a rapid high-altitude slope failure involving glacier ice, which generated a large mass of ice, rock, sediment, and water. The failure generated energy equivalent to that of an M5.2 earthquake (USGS, 2026). This material entered the Bhote Koshi River through Lhende River and rapidly propagated downstream, transforming into a sediment-laden flood and causing extensive damage to settlements, roads, bridges, hydropower facilities, and other infrastructure along the

Trishuli river valley (e.g., USGS, 2026).

Similar cascading disasters have occurred elsewhere in the Himalayan region. For example, the 2021 Chamoli disaster in the Indian Himalaya was initiated by a massive rock-ice avalanche that evolved into a highly mobile debris flow and flood, resulting in severe downstream damage and loss of life (Shugar et al., 2021). Likewise, the 2015 earthquake-triggered ice-rock avalanche in Nepal's Langtang Valley demonstrated the susceptibility of steep, glacierized Himalayan terrain to catastrophic ice–rock mass movements (Lacroix, 2016). On 16 August 2024, a catastrophic cascading glacial lake outburst flood (GLOF) devastated Thame Village in the Khumbu region of Nepal. The event was initiated by a rock avalanche entering Upper Ngole Cho, which generated a displacement wave and triggered the subsequent breaching of the downstream glacial lake, producing a highly destructive flood and sediment-laden flow (Maharjan et al., 2025). In 2025, one of the worst rock-ice avalanche occurred in Blatten, Switzerland (Farinotti et al., 2025; Yang et al., 2025), in which collapsed rock mass settled onto the glacier, destabilizing it and triggering a rock-ice avalanche eight days later. This time lag saved 300 people's life.

The 2026 event represents a typical cascading geohazard, in which an initial high-altitude slope failure, involving both bedrock and glacier ice, triggered a debris avalanche and debris flow that subsequently evolved into a destructive downstream flash flood. The cascading nature of the event resulted in impacts extending approximately more than 100 km far beyond the initial source area. This report presents a preliminary assessment of the disaster based on satellite imagery, covering the affected river corridor from the source area near the Nepal–China border downstream to Mairetar, approximately 30 km northwest of Kathmandu. Areas downstream of Mairetar were not analyzed because of limited satellite data availability. The GIS data generated through this assessment can be made available to support disaster response, rescue, and recovery activities. Please contact the first author to request access to the data. We conveyed our heartfelt condolences and support to the people affected by the disaster.

2. Method

We conducted a preliminary assessment of the disaster using satellite imagery. Pre-

and post-event imagery was compared to identify changes in the river channel and surrounding terrain, and inundated areas. The pre-event imagery consisted of satellite imagery from Microsoft Bing and Google Earth, while post-event imagery on August 27, 2026 included Planet imagery downloaded from OpenAerialMap (https://map.openaerialmap.org), Sentinel-2 Open image provided by the European Space Agency (https://www.esa.int/Applications/Observing_the_Earth/Copernicus/Sentinel-2/Nepal_flash_flood_imaged_by_satellites) and Landsat 9 satellite imagery obtained from Soar (https://soaratlas.com/). These datasets were used to identify the potential source area of the rock-ice avalanche, delineate the affected and inundated areas, and infer the possible sequence and processes of the event. In addition, the locations of settlements, roads, bridges, and hydropower facilities were overlaid on the affected areas using QGIS to assess the spatial distribution and potential extent of damage. The interpretation results may be subject to uncertainty due to the spatial resolution of the available satellite imagery and cloud cover, which may have obscured some affected areas.

3. Results

3.1 Pre-event conditions and inferred failure sequence

3.1.1 Geomorphological setting of the source area

The source area is located at the terminus of a glacier at an elevation of approximately 5,060 m a.s.l., on a steep, high-relief mountain slope comprising glacier ice and underlying bedrock (Fig. 1). The source area has a maximum width of approximately 1.8 km and, together with the initial flow path, covers approximately 7.8 km². The area is characterized by high relief, steep slopes, and a narrow, confined valley system (Fig. 1).

Examination of pre-event Google Earth imagery suggests that a small, shallow glacial lake was present near the lower terminus of the glacier (Figs. 1a and 2). Downstream of the lake, an apron-like accumulation surface composed of moraine and till extended toward the main Bhote Koshi River valley. Step-like features, possibly associated with differential glacier movement or localized deformation, were visible near the glacier terminus (Fig. 3). In addition, small step-like features were observed on exposed bedrock slabs immediately below the glacier terminus. Although their origin cannot be determined conclusively from satellite imagery alone, these features may

indicate localized slope deformation or displacement prior to the catastrophic failure.

3.1.2 Bedrock structure and slope preconditioning

The source area is further characterized by complex bedrock morphology and structural discontinuities. Two underlying rock blocks appear to form an overhanging structure, with their lateral margins apparently undercut by glacial erosion (Fig. 4). Such undercutting may have reduced the lateral and basal support of the rock mass. In addition, the exposed bedrock contains continuous and persistent fractures (Fig. 5), indicating the presence of pre-existing structural discontinuities within the slope. The exposed bedrock surfaces are not uniformly smooth and strongly polished, as might be expected from simple glacial abrasion, but instead are characterized by fractured and irregular surfaces. This morphology suggests that, in addition to glacial abrasion and localized plucking, structural controls such as joints and bedding planes, together with frost weathering under periglacial climate, may have contributed to the progressive weakening and disintegration of the rock mass.

These pre-existing discontinuities may also have facilitated the infiltration of snowmelt and glacier meltwater into the slope, promoting water penetration and progressive weakening along fractures and bedding planes. The brownish coloration observed along some fractures (Fig. 5) may indicate oxidation associated with water–rock interactions, although this interpretation requires further verification.

3.1.3 Glacier deformation and progressive destabilization

The glacier itself also shows evidence of active deformation. Prominent crevasses developed on the glacier surface suggest the presence of substantial extensional strain associated with glacier flow. Such deformation may have contributed to the mechanical instability of the glacier terminus and may indicate that parts of the ice mass were prone to collapse or break-off. Furthermore, recent glacier retreat and ice thinning may have played an important role in destabilizing the slope. The reduction in glacier thickness could reduce the mechanical support or buttressing previously provided by the glacier to adjacent bedrock slopes. Progressive loss of this support, combined with glacial erosion, structural discontinuities, weathering, and meltwater infiltration, may have progressively preconditioned the slope for failure.

3.1.4 Possible precursory activity and failure mechanism

According to local residents, muddy flows had reportedly been observed for approximately four days before the main event. Although this information requires further verification, one possible explanation is that a series of small-scale collapses occurred around the glacier terminus during this period. Sediment and rock generated by these collapses may have entered the small glacial lake, potentially contributing to the muddy flows observed by local residents.

The observations described above suggest that the catastrophic event may have resulted from a complex coupled failure involving both glacier ice and bedrock. Under conditions of progressive glacier thinning and retreat, the loss of ice support may have destabilized the underlying and adjacent rock masses, while pre-existing fractures and bedding planes may have provided potential failure surfaces.

The final catastrophic failure appears to have involved the large-scale collapse of the glacier terminus together with the underlying bedrock. However, it remains unclear whether the glacier and bedrock failed simultaneously or in rapid succession. Following detachment, the resulting ice–rock mass rapidly descended the slope, progressively entraining additional bedrock-derived material, sediment, and potentially water along its flow path. The steep relief and U-shaped, confined valley likely facilitated rapid downslope movement and efficient transfer of the failed material toward the main channel.

Upon reaching the main channel at approximately 2,930 m a.s.l., the highly mobile mass continued downstream as a sediment-rich flow. During its downstream propagation, the flow caused extensive channel erosion and further entrainment, transport, and deposition of sediment, substantially modifying the river corridor.

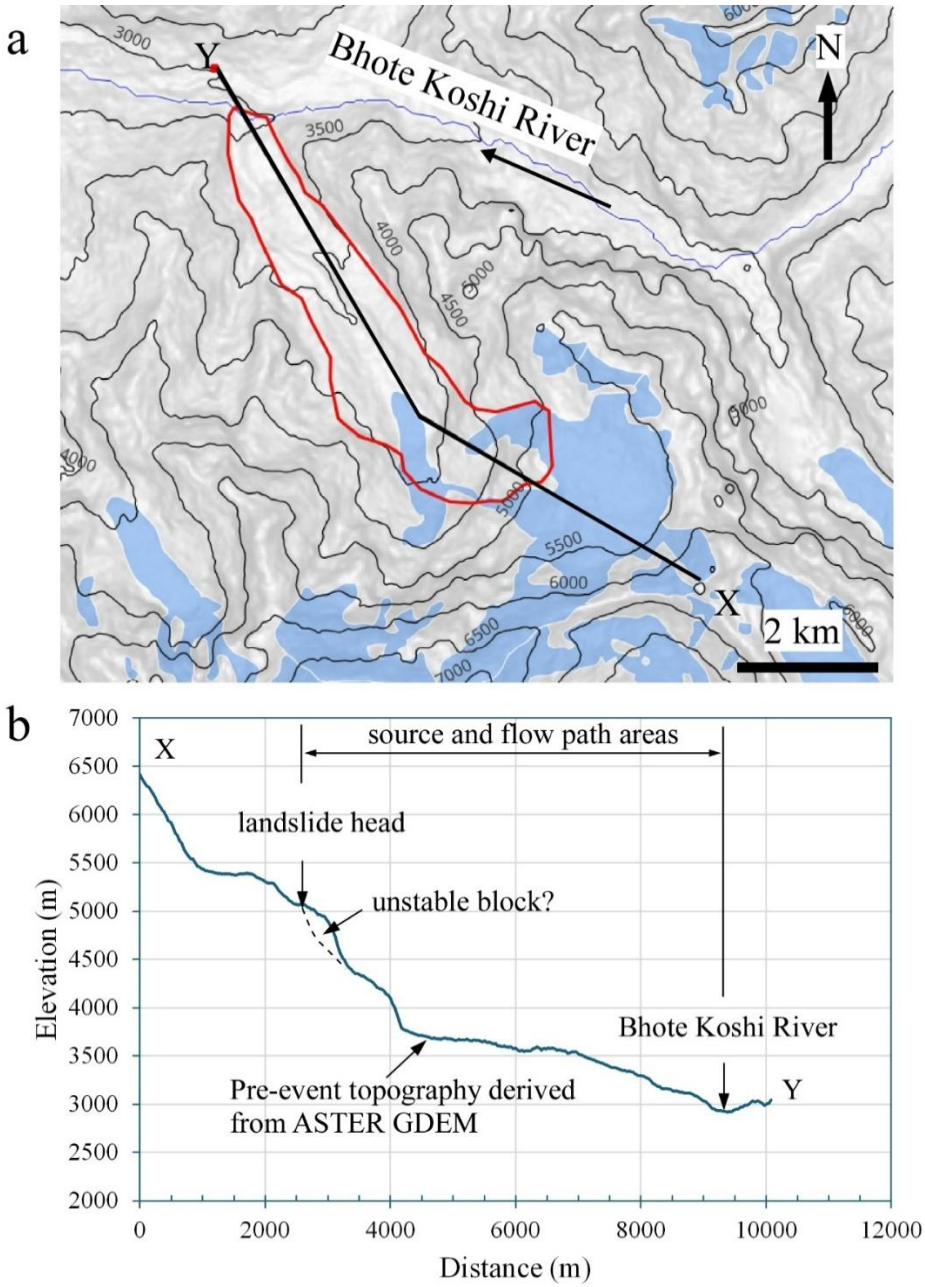

Fig. 1 Pre-event topography and longitudinal profile of the 2026 rock-ice avalanche source area and flow path. (a) Topographic map showing the landslide source and initial flow-path areas (red polygon). The black line from X to Y indicates the transect used to construct the longitudinal profile. Blue polygons indicate the distribution of glacierized areas based on Pfeffer et al. (2014). Contour lines and the underlying slope image were derived from the ASTER Global Digital Elevation Model (GDEM). (b) Longitudinal elevation profile along the X–Y transect, showing the landslide head and inferred unstable block.

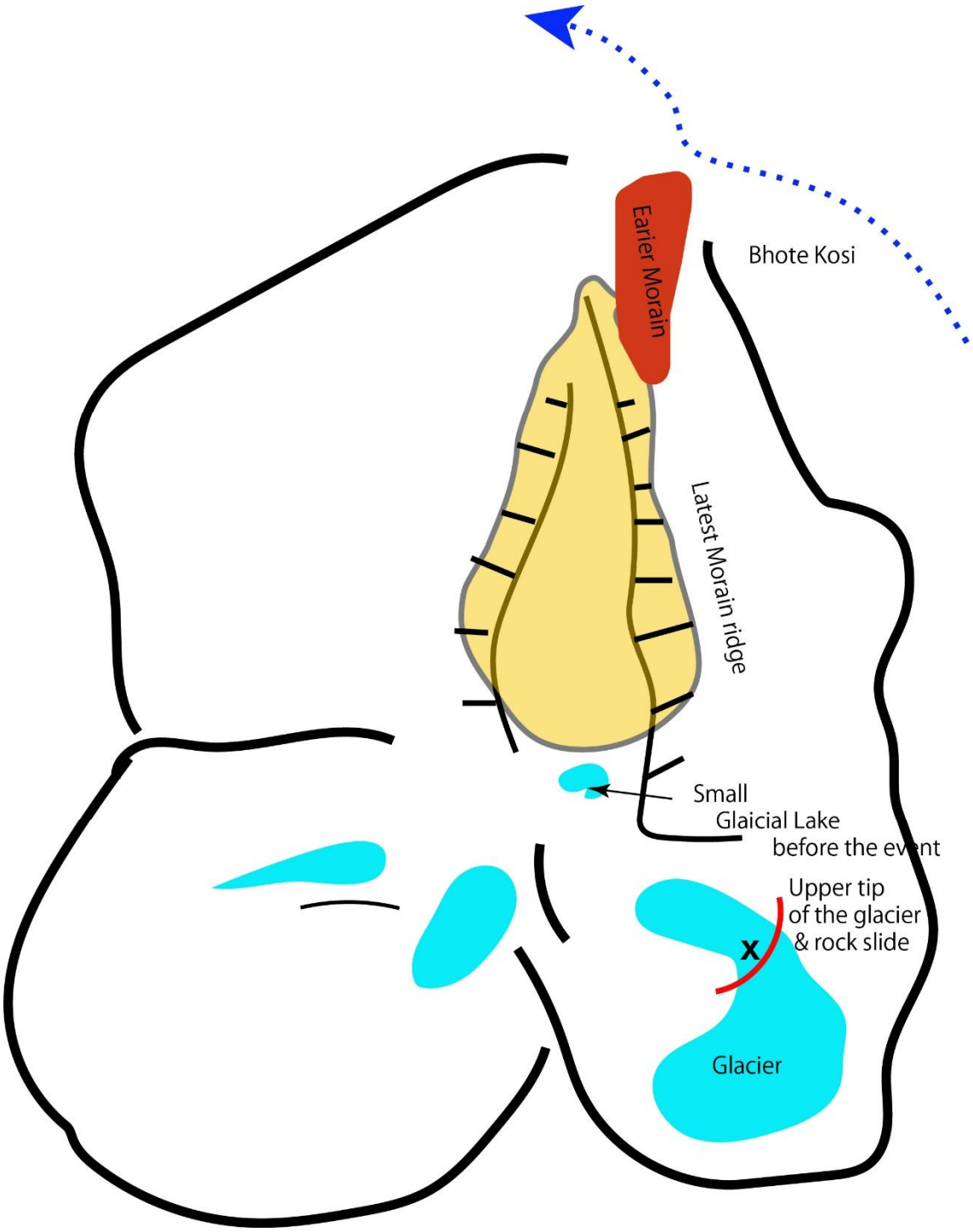

Fig. 2 Pre-event Google Earth imagery of the source area and flow path of the 2026 rock-ice avalanche. The schematic illustration is not drawn to scale.

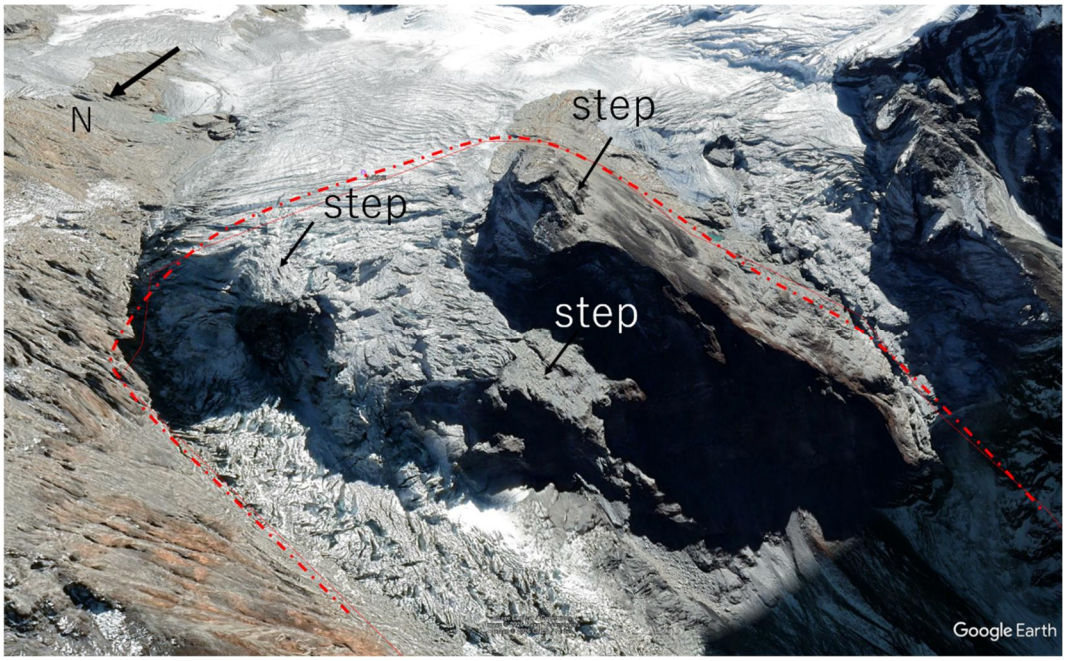

Fig. 3 Topography of the source area prior to the 2026 rock-ice avalanche. The red dashed line indicates the source area the 2026 rock-ice avalanche. (Google Earth imagery acquired on November 28, 2020)

(Note: We have revised Fig. 3 of the original report posted on September 9 because the information regarding the photo location was incorrect.)

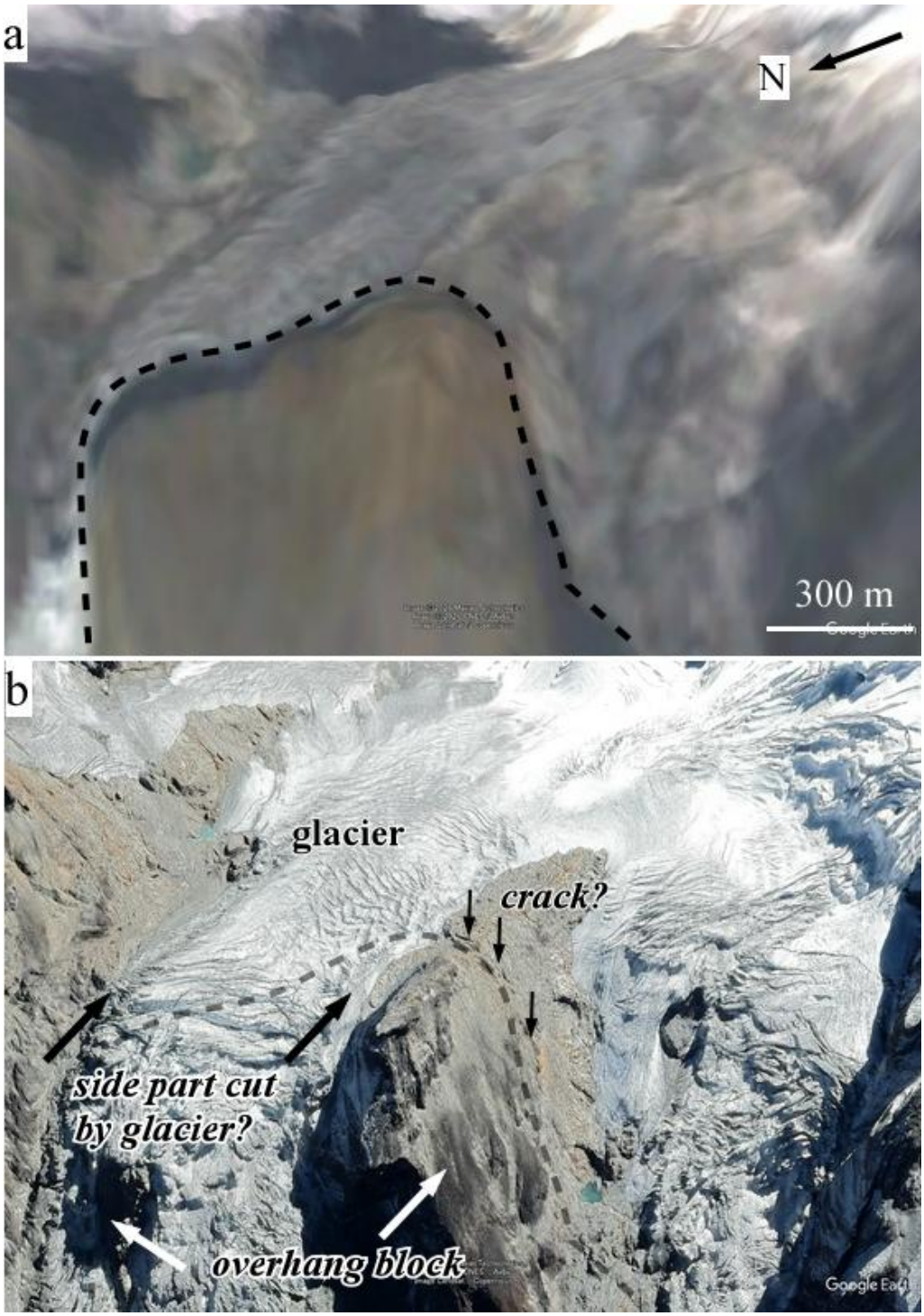

Fig. 4 Close-up views of the source area before and after the event. (a) Landsat 9 satellite imagery acquired after the event, obtained from Soar (https://soaratlas.com/). (b) Google Earth imagery acquired on December 1, 2017, showing the pre-event condition. The dashed black line indicates the landslide extent.

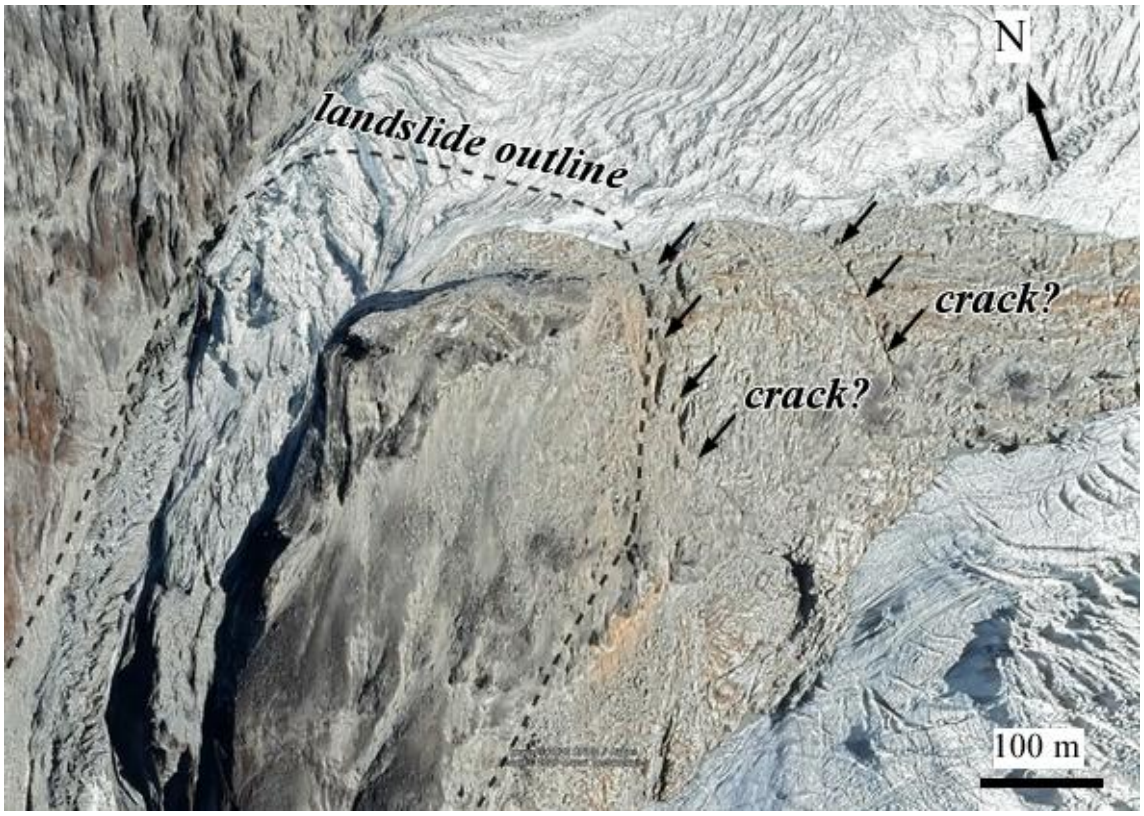

Fig. 5 Close-up view (Google Earth imagery acquired on December 1, 2017) of the source area before the event. The exposed underlying bedrock appears to contain continuous or persistent cracks, along which rock color changed to brownish suggesting the intense weathering occurred.

3.2 Formation of impounded lakes and secondary slope failure

3.2.1 Formation of the upstream impounded lake

Two impounded lakes subsequently formed immediately downstream of the failure source and near the confluence between the U-shaped valley and the V-shaped valley of the Bhote Koshi River (Fig. 6). These lakes were not observed immediately after the initial failure. Based on satellite imagery acquired on 28 August, the upstream impounded lake was approximately 600 m long and 400 m wide, with an area of approximately 190,000 m^2. The downstream lake was approximately 900 m long and 260 m wide, with an area of approximately 120,000 m^2.

The formation process of the upstream impounded lake is tentatively interpreted based on the observed distribution of sediment deposits. The middle to upper reaches of

the valley within the recent moraine were extensively buried by material derived from the 2026 failure. It is therefore inferred that the accumulation of debris in the upper part of this valley obstructed the drainage and resulted in the formation of the upstream impounded lake.

3.2.2 Flow interaction with the moraine system

Near the confluence between the U-shaped and V-shaped valleys, a moraine-like landform, which is presumed to be connected to the older moraine, separates the main river from its tributary. This feature forms an east–west-oriented ridge, with a relative height of approximately 150 m above the valley floor of the main river and a maximum width of approximately 300 m. The flow originating from the failure source appears to have travelled northward and overtopped this ridge-like moraine. It subsequently reached the upper part of the opposite northern valley slope, approximately 300–400 m above the valley floor (Fig. 6). These observations further demonstrate the exceptional mobility and run-up height of the flow.

3.2.3 Secondary slope failure and formation of the downstream impounded lake

A large secondary landslide, covering an area of more than 340,000 m², was identified on the western side of the confluence (Fig. 6). Satellite imagery acquired on 27 August shows that the slope was still covered by vegetation and no landslide scar was visible. In contrast, imagery acquired on 28 August clearly shows a newly developed landslide scar, indicating that the failure occurred between 27 and 28 August. This temporal sequence suggests that the landslide was not directly formed during the initial upstream failure on 26 August. Instead, it may represent a secondary slope failure caused by progressive destabilization following the passage of the flood and debris flow. Substantial erosion at the base of the mountain slope during the 26 August event may have undercut and weakened the slope, leading to subsequent failure on the right bank between 27 and 28 August.

The large volume of sediment generated by this secondary landslide may then have partially or completely blocked the main river, contributing to the formation of the downstream impounded lake. This sequence represents an additional cascading process in which the initial glacier–bedrock failure triggered a high-energy sediment-laden flow,

which subsequently caused channel and slope erosion, leading to a delayed secondary landslide and further river blockage.

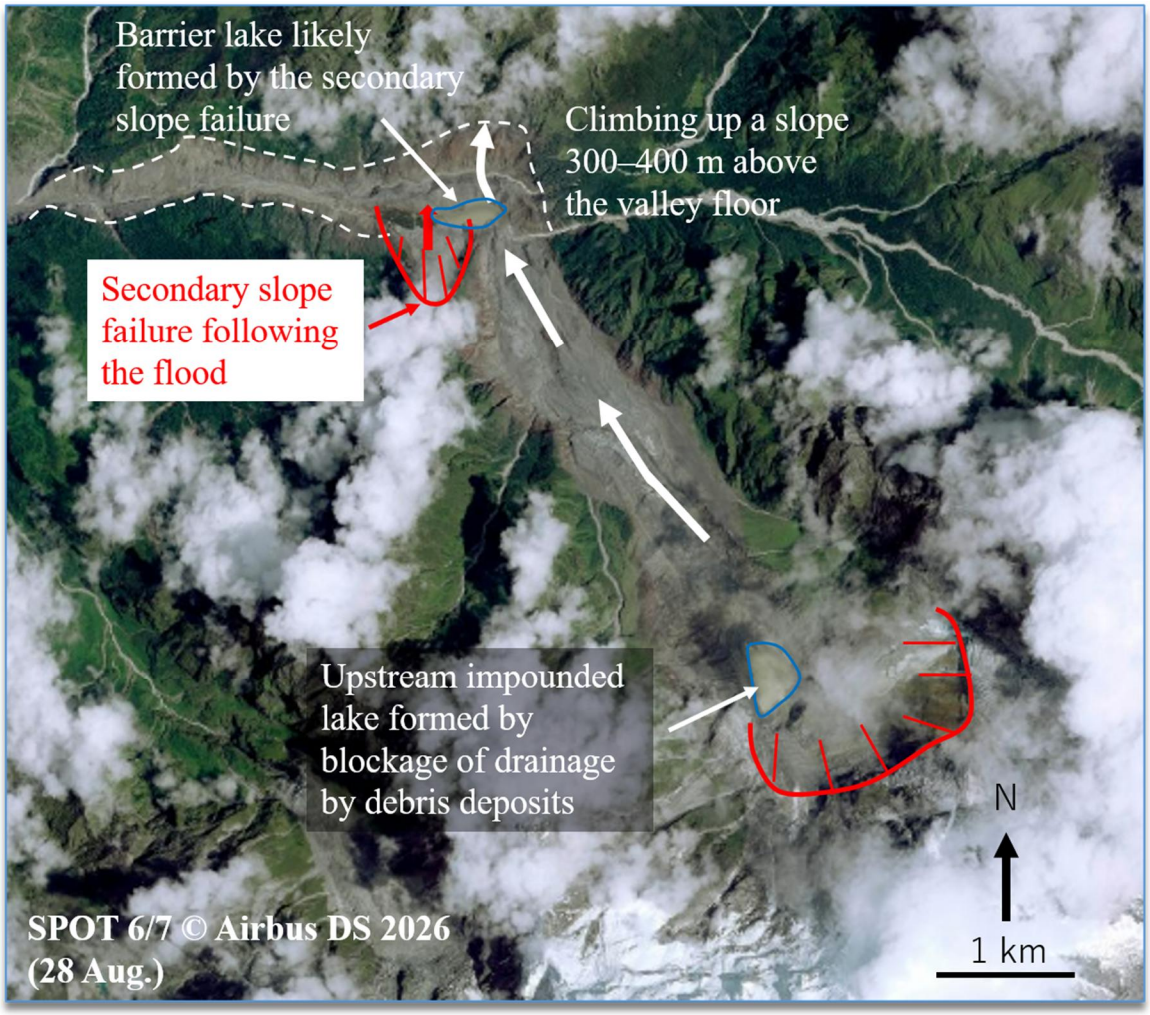

Fig. 6 Formation of upstream and downstream impounded lakes and the occurrence of a secondary slope failure following the 2026 disaster. The satellite image was acquired on 28 August 2026 and downloaded from Airbus Intelligence (https://space-solutions.airbus.com/).

3.3 Downstream geomorphic changes and infrastructure impacts

3.3.1 Channel widening, erosion, and sediment deposition

The preliminary analysis revealed extensive geomorphic and land-cover changes along the affected river corridor, including inundation, riverbank erosion, channel widening, lateral channel migration, and widespread sediment and debris deposition. Extensive bank erosion substantially expanded the active river corridor, while large

volumes of sediment and debris were deposited within the channel and across adjacent floodplains, locally modifying the pre-event channel configuration.

A detailed comparison of pre- and post-event channel conditions along an approximately 40-km reach of the Trishuli River, from Syaphru Besi (approximately 1,430 m a.s.l.) to Trishuli (approximately 530–540 m a.s.l.) (Fig. 7), further demonstrates the magnitude of these geomorphic changes. Channel widths increased at all measured locations, with an average increase of approximately 4.5 times compared with pre-event conditions (Table 1). The magnitude of widening varied considerably among locations, reflecting differences in valley morphology and the availability of sediment for erosion and deposition.

Even within deeply incised V-shaped valleys bordered by steep, predominantly bedrock slopes, the channel width increased by approximately 1.7–7 times. These changes were accompanied by substantial sediment deposition and riverbed aggradation. Comparison of pre- and post-event channel positions suggests that, in some V-shaped valley sections, the riverbed may have been elevated by approximately 40–80 m relative to its pre-event level. Along an approximately 20-km-long section, the valley floor descends by approximately 630 m, corresponding to an average channel gradient of about 2°. Despite this relatively steep and confined setting, the large volume and high mobility of the sediment-laden flow enabled extensive deposition that temporarily filled the valley.

The high-energy flow also caused severe erosion of valley-side slopes. Trees growing at elevations well above the area normally affected by river flow were stripped from the slopes, indicating that the flow reached exceptionally high levels. This erosion likely resulted in further entrainment of sediment and wood logs, increasing both the volume and erosive capacity of the flow as it propagated downstream.

3.3.2 Downstream Flooding and Channel Modification

Downstream of Betrawati, the sediment-laden flood spread beyond the confined valley and inundated terrace surfaces and valley-floor plains. At Trishuli Bazar, the flow appears to have reached areas more than 15 m above the normal river level. Progressive riverbed aggradation may have raised the water and sediment surface and forced subsequent flows toward the valley margins, promoting bank erosion and lateral channel

migration. In relatively gentle-gradient tributaries, the main flow locally propagated upstream, resulting in backflow and sediment deposition. However, no clear channel blockage was identified within the tributary reaches examined in the satellite imagery acquired on 27 August. These observations indicate that the downstream impacts were controlled not only by the initial flood magnitude but also by progressive changes in channel geometry and sediment accumulation during flow propagation.

3.3.3 Damage to settlements and infrastructure

The extensive geomorphic changes caused severe damage to settlements and infrastructure. The expansion of the active river corridor affected adjacent settlements, agricultural land, roads, bridges, and hydropower facilities (Figs. 8 and 9). Based on satellite imagery, at least 2,587 buildings, 21 bridges, 12 suspension bridges, and 7 hydropower facilities were identified as destroyed. Although road damage was not systematically included in the present mapping, widespread disruption of the road network was evident from the available satellite imagery. Between the Trishuli 3A Hydroelectric Project and Syaphru Besi, a road is located on a relatively high surface along the left bank of the Trishuli River. In contrast, roads closer to the river channel, particularly between Syaphru Besi and the Trishuli 3A intake structure, appear to have been constructed along the lower part of the valley flank following the 2015 Gorkha earthquake.

Although some of these roads are located approximately 50–100 m above the pre-event riverbed, they appear to lie near the upper limit of the area affected by the flood and sediment-laden flow. This suggests that the event produced a substantial increase in flow depth and inundation height within the confined V-shaped valley. Consequently, some road sections may have experienced overtopping, erosion or washout of road surfaces and foundations, slope failures, and sediment deposition. Severe erosion and failure of road foundations and embankments were also observed at several locations, potentially contributing to prolonged disruption of transportation and access.

3.3.4 Potential secondary and cascading hazards

In addition to the direct damage to infrastructure, numerous potentially unstable landslides are distributed along the affected valley slopes. In some locations, erosion

caused by the flood may have undercut the lower parts or toes of these landslides, potentially reducing their stability. Such conditions could promote secondary slope failures and additional sediment movement during subsequent rainfall events or flooding. Furthermore, continued channel instability, riverbank erosion, and sediment redistribution may increase the likelihood of additional damage to roads, settlements, bridges, and other infrastructure. These observations indicate that the impacts of the 2026 event may continue beyond the initial disaster through a series of secondary and cascading processes. These potential hazards should therefore be considered in future field investigations, reconstruction planning, and risk assessments.

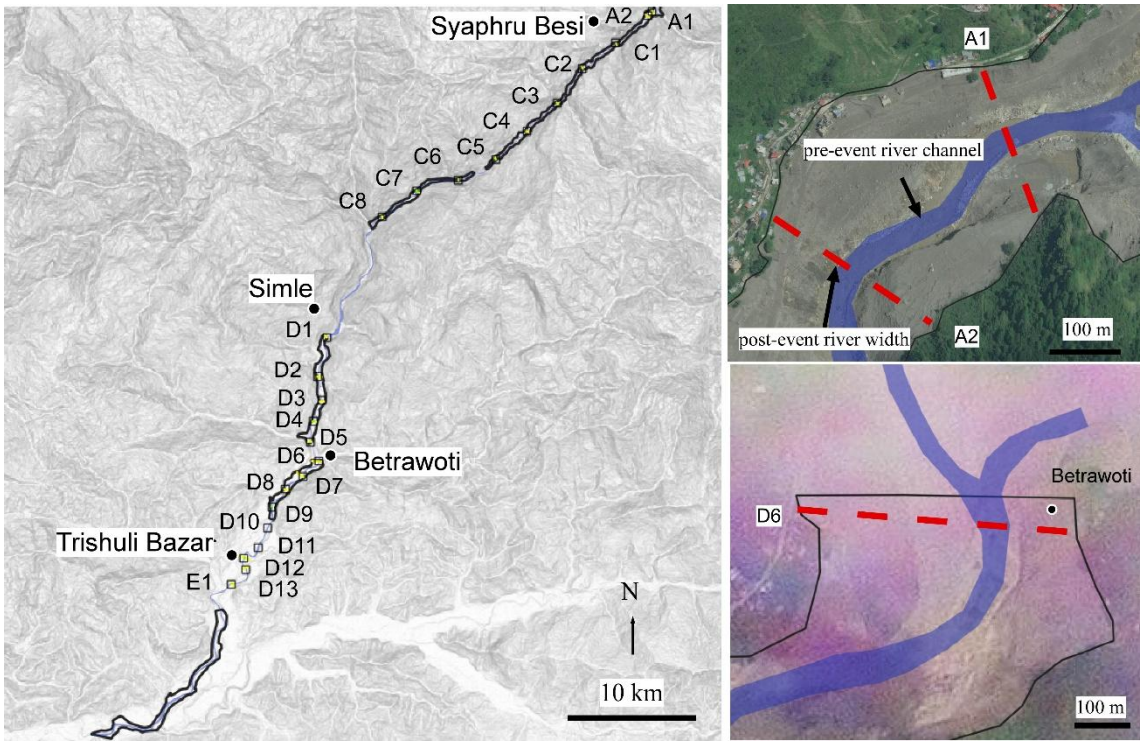

Fig. 7. Locations of cross sections used to measure changes in channel width along the Trishuli River between Syaphru Besi and Trishuli Bazar before and after the 2026 disaster. Results are summarized in Table 1.

Table 1. Pre- and post-event changes in channel width along the Trishuli River from Syaphru Besi to Trishuli Bazar.

Section	Location	Width(m) before the flood (wb)	Width(m) after the flood (wa)	Expansion ratio(wa/wb)	Approximate pre-event riverbed elevation (m asl.)	Morphology
A1	Syaphru Besi	70	234	3.34	1430	
A2		40	280	7.00	1430	
C1		30	170	5.67	1370	
C2		40	210	5.25	1340	V-shaped valley
C3		50	170	3.40	1270	
C4		30	190	6.33	1220	
C5		60	160	2.67	1170	
C6		50	120	2.40	1080	
C7		140	240	1.71	1020	
C8		60	160	2.67	940	
D1	Simle	70	210	3.00	730	
D2		110	310	2.82	690	
D3		110	300	2.73	660	
D4		90	250	2.78	640	
D5		70	200	2.86	620	
D6	Betrawoti	60	560	9.33	610	Confluence
D7		90	420	4.67	590	
D8		70	310	4.43	580	
D9		60	240	4.00	570	
D12	Trisuli Bazar	70	530	7.57	540	
D13	Trisuli Bazar	45	290	6.44	535	
E1	Trishuli/Bidur	40	310	7.75	530	
				average: 4.5		

Note: Measurement interval: A1-C8 and D-1-D2 (~every 2km), C8-D1: (ca. 6km), D2-E1 (~every 1km)

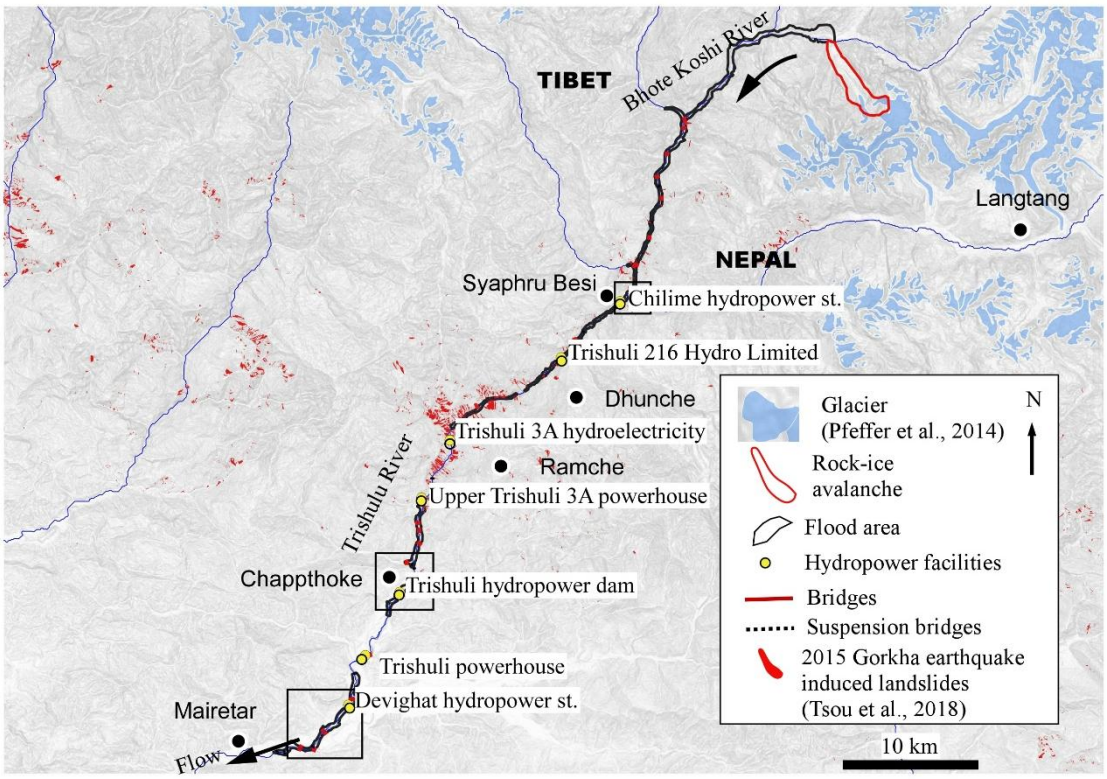

Fig. 8 Distribution of areas affected by the rock-ice avalanche and subsequent debris flow and flash flood, including damaged infrastructure. Blue polygons indicate the distribution of glacierized areas based on Pfeffer et al. (2014). The underlying slope map was derived from the ASTER Globe GDEM. The interpretation is subject to uncertainty owing to the spatial resolution of the available satellite imagery and cloud cover, which may have obscured some affected areas. Furthermore, areas downstream of Mairetar were excluded from the analysis because of limited satellite data availability. Squares indicate areas shown in greater detail in Fig. 9 from upstream to downstream.

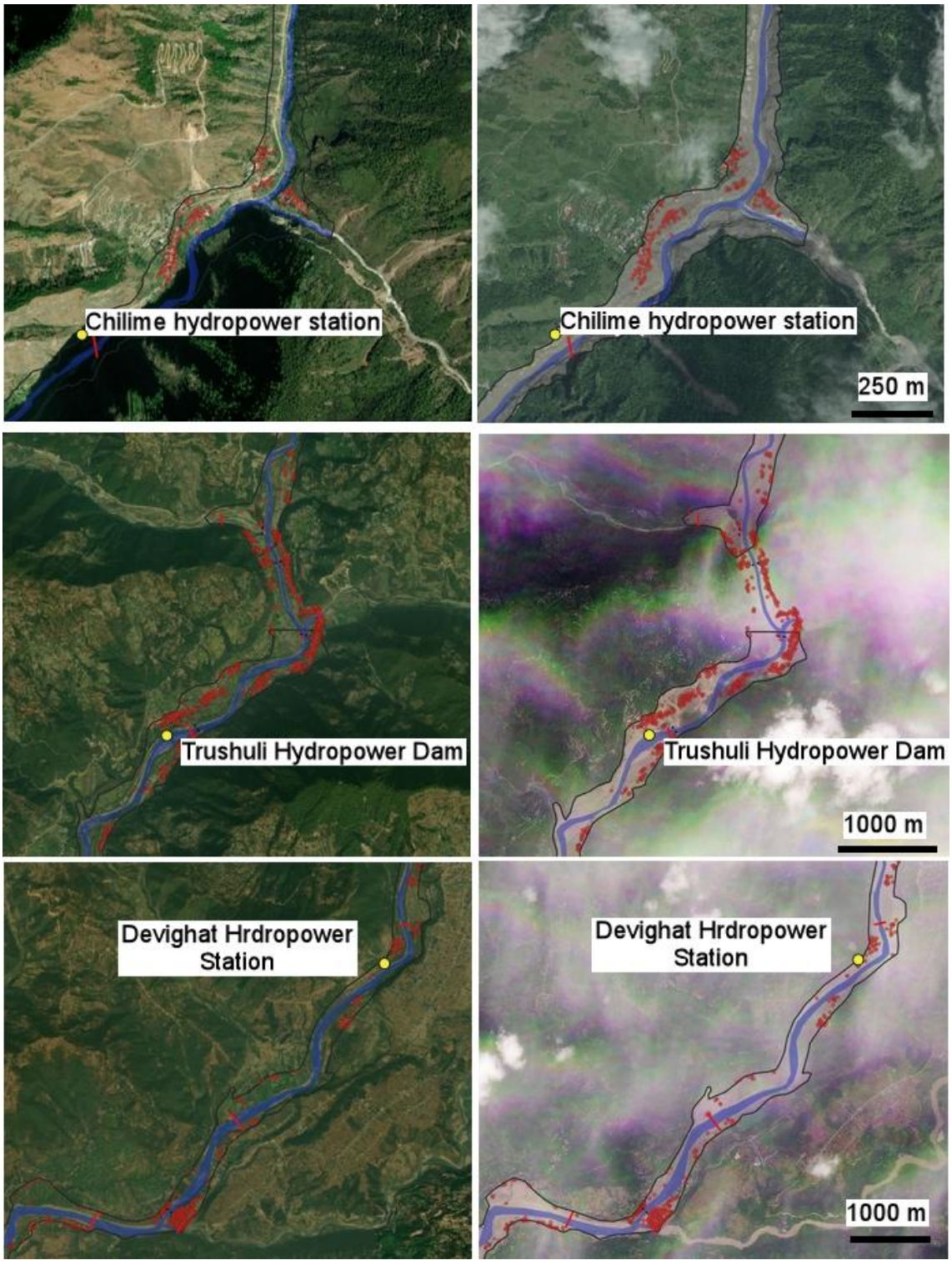

Fig. 9 Close-up satellite images of the affected areas before (left panels) and after (right panels) the event. Pre-event imagery consisted of satellite images from Microsoft Bing, whereas post-event imagery acquired on August 27, 2026, consisted of Planet imagery obtained through OpenAerialMap (https://map.openaerialmap.org). Red points indicate

the locations of destroyed buildings. Blue polygons indicate the river channel before the event. Other symbols and legends are the same as those in Fig. 8

4. Summary and recommendations

4.1 Summary

The 2026 disaster developed as a complex cascading process extending from the high-altitude source area to downstream river valleys. Progressive glacier retreat, ice thinning, bedrock weathering, and structural discontinuities may have progressively destabilized the source slope, eventually resulting in a coupled ice–bedrock failure. The failed mass rapidly transformed into a highly mobile debris avalanche and subsequently into debris flow and sediment-rich water flow as a flash flood through progressive entrainment of water, sediment, and additional material along its flow path. The flow caused extensive erosion, sediment deposition, channel widening, and riverbed aggradation over a long downstream reach. These geomorphic changes resulted in severe damage to settlements and infrastructure and may have triggered additional slope failures and river blockages. The event therefore demonstrates the importance of considering the entire chain of processes, from high-altitude glacier and slope instability to downstream debris flow and flooding, sediment transport, and secondary hazards. At the same time, the loss of bridges and destruction of power-generation facilities not only directly threaten human lives but also disrupt social and economic activities and affect the daily lives of residents across a wide area.

4.2 Recommendations

Further investigation is needed to better understand the causes and consequences of the 2026 disaster. First, detailed field investigations should be conducted in the source area to clarify the failure mechanism, particularly to assess the influence of climate-change-related factors and associated roles of glacier retreat, ice thinning, bedrock structure, fracturing, and meltwater dynamics. Second, remaining unstable ice, rock, and sediment should be assessed because they may cause secondary landslides, debris flows, or floods. Third, continuous monitoring using satellite imagery, UAV surveys, and ground-based observations is recommended to detect changes in unstable slopes and glaciers. There are also concerns about secondary river blockages caused by new slope

failures along the riverbanks in the upper reaches. Finally, future hazard assessments should consider the entire cascading process, from glacier and slope failures in high-altitude areas to downstream flooding and sediment deposition. Reconstruction and land-use planning should also consider possible future channel changes and extreme events. This event highlights the need for integrated monitoring and risk assessment of glacier-related and cascading hazards across national borders in the Himalayan region, especially under the influence of climate change.

References

1. Farinotti, D., Matthias, H., Jacquemart, M., and Werder, M. (2025) Fact sheet for the now-collapsed Birchgletscher, Switzerland. ETH, WSL.
2. Lacroix, P. (2016) Landslides triggered by the Gorkha earthquake in the Langtang valley, volumes and initiation processes, Earth Planets Space, 68:46. https://doi.org/10.1186/s40623-016-0423-3
3. Maharjan, S. B., Sherpa, T. C., & Shrestha, A. B. (2025). Thame Valley Glacial Lake Outburst Flood 2024: Causes, impacts and future risks. International Centre for Integrated Mountain Development (ICIMOD) and National Disaster Risk Reduction and Management Authority (NDRRMA), Kathmandu, Nepal. 39 pp. https://doi.org/10.53055/ICIMOD.1101
4. Pfeffer WT, Arendt AA, Bliss A, Bolch T, Cogley JG, Gardner AS, Hagen JO, Hock R, Kaser G, Kienholz C, Miles ES, Moholdt G, Molg N, Paul F, Radic V, Rastner P, Raup BH, Rich J, Sharp MJ, Andeassen LM, Bajracharya S, Barrand NE, Beedle MJ, Berthier E, Bhambri R, Brown I, Burgess DO, Burgess EW, Cawkwell F, Chinn T, Copland L, Cullen NJ, Davies B, De Angelis H, Fountain AG, Frey H, Giffen BA, Glasser NF, Gurney SD, Hagg W, Hall DK, Haritashya UK, Hartmann G, Herreid S, Howat I, Jiskoot H, Khromova TE, Klein A, Kohler J, Konig M, Kriegel D, Kutuzov S, Lavrentiev I, Le Bris R, Li X, Manley WF, Mayer C, Menounos B, Mercer A, Mool P, Negrete A, Nosenko G, Nuth C, Osmonov A, Pettersson R, Racoviteanu A, Ranzi R, Sarikaya MA, Schneider C, Sigurdsson O, Sirguey P, Stokes CR, Wheate R, Wolken GJ, Wu LZ, Wyatt FR, and The Randolph Consortium (2014) The Randolph Glacier Inventory: a

globally complete inventory of glaciers, J Glaciol., 60, 537–552.

5. Shugar, D.H., Jacquemart, M., Shean, D., Bhushan, S., Upadhyay, K., Sattar, A., Schwanghart, W., McBride, S.K., Van Wyk de Vries, M., Mergili, M., Emmer, A., Deschamps-Berger, C., McDonnell, M., Bhambri, R., Allen, S., Berthier, E., Carrivick, J., Clague, J., Dokukin, M., Dunning, S., Frey, H., Gascoin, S., Haritashya, U., Huggel, C., Kaab, A., Kargel, J., Kavanaugh, J., Lacroix, P., Petley, D., Rupper, S., Azam, M., Cook, S., Dimri, A., Eriksson, M., Farinotti, D., Fiddes, J., Gnyawali, K., Harrison, S., Jha, M., Koppes, M., Kumar, S., Leiness, S., Majeed, U., Mai, S., Muhuri, A., Noetzli, J., Paul, F., Rashid, I., Sain, K., Steiner, J., Ugalde, F., Watson, C., and Westoby, M. (2021) A massive rock and ice avalanche caused the 2021 disaster at Chamoli, Indian Himalaya, Science, eabh4455, 15 p., https://doi.org/10.1126/science.abh4455.
6. Tsou, C.-Y., Higaki, D., Chigira, M., Yagi, H., Dangol, V., Amatya, S.C., Hayashi, K., Kato, H. (2018) Topographic characteristics of landslides triggered by the 2015 Gorkha earthquake, Nepal. Journal of Nepal Geological Society, Vol. 55 (Sp. Issue), pp. 69–75.
7. USGS (2026) 2026 Nepal Debris Avalanche and Flash Flood, https://www.usgs.gov/programs/landslide-hazards/science/2026-nepal-debris-avalanche-and-flash-flood (accessed date: 2026.9.5)
8. Yang, D., Qiu, H., Quevedo, R.P., Liu, Y. & Glade, T. (2025). Birchgletscher rock-ice avalanche burying the village of Blatten on 28 May 2025, Valais, Switzerland, Landslides, doi: 10.1007/s10346-025-02656-y.